

Article

Mine Surface Settlement Prediction Based on Optimized VMD and Multi-Model Combination

Liyu Shen ^{1,2,3}  and Weicai Lv ^{1,2,3,*}¹ School of Geomatics, Anhui University of Science and Technology, Huainan 232001, China² Coal Industry Engineering Research Center of Mining Area Environmental and Disaster Cooperative Monitoring, Huainan 232001, China³ Key Laboratory of Aviation-Aerospace-Ground Cooperative Monitoring and Early Warning of Coal Mining-Induced Disasters of Anhui Higher Education Institutes, KLAHEI, Huainan 232001, China

* Correspondence: 2021201618@aust.edu.cn

Abstract: The accurate prediction of mining area surface deformation is essential to preventing large-scale coal mining-related surface collapse and ensure safety and daily life continuity. Monitoring subsidence in mining areas is challenged by environmental interference, causing data noise. This paper employs the Sparrow Search Algorithm, which integrates Sine Cosine and Cauchy mutation (SCSSA), to optimize variational mode decomposition (VMD) and combine multi-models for prediction. Firstly, SCSSA is employed to adaptively determine the parameters of VMD using envelope entropy as the fitness value. Subsequently, the VMD method optimized using SCSSA adaptively decomposes the original mining area subsidence data sequence into various sub-sequences. Then, SCSSA-VMD is applied to adaptively decompose the original mining subsidence data sequence into multiple sub-sequences. Meanwhile, using sample entropy, the sub-sequences are categorized into trend sequences and fluctuation sequences, and different models are employed to predict sub-sequences at different frequencies. Finally, the prediction results from different sub-sequences are integrated to obtain the final prediction of mining area subsidence. To validate the predictive performance of the established model, experiments are conducted using GNSS monitoring data from the 110801 working face of Banji Coal Mine in Bozhou. The results demonstrate the following: (1) The hybrid model enhanced the prediction accuracy and trends by decomposing the data and optimizing the parameters with VMD. It outperformed single models, reducing errors and improving predictive trends. (2) The hybrid model significantly improved the prediction accuracy for subsidence data at work surface monitoring stations. It is particularly effective at critical subsidence points, making it a valuable reference for safety in mining operations.

Keywords: GNSS monitoring station; variational mode decomposition; multi-model; ground subsidence prediction; hybrid model



Citation: Shen, L.; Lv, W. Mine Surface Settlement Prediction Based on Optimized VMD and Multi-Model Combination. *Processes* **2023**, *11*, 3309. <https://doi.org/10.3390/pr11123309>

Academic Editors: Abbas Abbaszadeh Shahri, Mahjoub Himi and Carlos Sierra Fernández

Received: 18 October 2023

Revised: 20 November 2023

Accepted: 23 November 2023

Published: 28 November 2023



Copyright: © 2023 by the authors. Licensee MDPI, Basel, Switzerland. This article is an open access article distributed under the terms and conditions of the Creative Commons Attribution (CC BY) license (<https://creativecommons.org/licenses/by/4.0/>).

1. Introduction

Energy serves as the fundamental pillar supporting a nation's prosperity and sustainable economic development [1]. Coal has consistently served as a primary energy source in China. For the sustainable development of the national economy, it is imperative to judiciously develop coal resources and ensure their secure and consistent supply. However, as mining areas expand, surface cracks emerge, posing significant threats to critical infrastructure situated above these regions, including cracking and subsidence. The extensive land subsidence induced by large-scale coal mining has led to the creation of coal mining subsidence areas, causing irreparable harm to the original ecological environment and structures within the mining region. To alleviate the adverse consequences of surface subsidence and deformation resulting from mining-induced voids, engaging in subsidence monitoring, analyzing monitoring data, and promptly and accurately comprehending subsidence patterns are essential. This is vital for effectively mitigating diverse geological

hazards resulting from mining-induced subsidence. Therefore, comprehensive research on subsidence patterns due to mining-induced surface subsidence, along with the application of scientific monitoring techniques and predictive models, is crucial for ensuring the sustainable development of the coal industry [2].

The rapid advancement in engineering construction has led to an increased focus on deformation-related concerns. Establishing a deformation monitoring technology that is both safe and reliable holds immense significance. To ensure the safety of mining operations and reduce geological hazards caused by stress and subsidence resulting from mining, high-precision surface deformation monitoring of mining areas is indispensable [3]. Presently, prevalent deformation-monitoring technologies encompass geometric leveling measurement technology [4], three-dimensional laser scanning technology [5], synthetic aperture radar differential interferometry measurement technology [6], and GNSS measurement technology [7]. With the progression of GNSS technology, its application in monitoring surface subsidence, landslides, dam deformations, and various other deformation aspects within mining areas has become widespread [8]. GNSS technology offers notable advantages, including high automation, rapid data acquisition, and exceptional accuracy. The utilization of GNSS technology for automated monitoring eliminates the necessity for monitoring stations to have a direct line of sight to each other. Each monitoring station can conduct observations independently, enabling the establishment of real-time monitoring networks. These networks facilitate the acquisition of deformation information, providing a comprehensive understanding of surface subsidence patterns. Faced with complex deformation processes, many scholars have conducted a series of studies on deformation prediction methods, leading to the widespread development of various theoretical models, such as GM(1,1) [9], Kalman filtering models [10], time series models [11], and neural network models [12]. However, as research has progressed, many scholars have found that using a single prediction model often had its limitations and does not comprehensively reflect subsidence patterns, making it less suitable for complex subsidence systems. When predicting surface subsidence using GNSS automated monitoring systems that include various random interference factors (such as mining depth, mining thickness, coal seam dip angle, mining speed, etc.), it is challenging to achieve high accuracy using a single prediction method. Therefore, seeking a combination prediction model that integrates the advantages of multiple models and effectively improves prediction accuracy is of significant importance. Without a doubt, combined prediction has become a popular research direction in the field of deformation prediction. J.M. Bates and C.W.J. Granger [13] first proposed the concept of a combined model, combining single prediction models using the method of minimum variance, greatly improving prediction accuracy. Du et al. [14] constructed a composite prediction model for open-pit slope deformation by combining an adaptive network fuzzy inference system and a support vector machine. Han et al. [15] established the SA-RELM model based on time series, achieving improved accuracy in ground subsidence prediction for excavation. Xu et al. [16] constructed an ARIMA-LSTM model to predict nonlinear feature data in dam deformations. Kim et al. [17,18] employed machine learning algorithms to effectively predict tunnel surface settlement, enhancing the prediction capabilities for surface settlement in urban tunnel construction sites under complex excavation conditions. In addition, the use of combination models with different machine learning methods and various optimization algorithms for predicting ground vibrations caused by blasting and tunnel excavation-induced surface settlement has found applications, effectively improving the prediction of ground settlement [19–25].

Utilizing different preprocessing models to decompose or filter data can effectively segregate nonlinear data into more regular and stable sub-sequences or eliminate spurious features with minimal correlation, thus enhancing model accuracy [26]. Presently, the spectrum of effective information extraction and denoising methods for long-term complex sequential data primarily encompasses wavelet analysis [27], empirical mode decomposition (EMD) [28], local mean decomposition (LMD) [29], and variational mode decomposition (VMD) [30]. In comparison to other methodologies like EMD and LMD,

VMD adeptly circumvents mode mixing, over-enveloping, boundary effects, and similar challenges. It demonstrates robust noise resistance and higher operational efficiency, along with exceptional precision in decomposing complex data and resilience to interference. These characteristics permit improved data decomposition. The determination of parameters and the quadratic penalty factor in the VMD method significantly affect the decomposition results [31]. VMD parameters are often determined through empirical judgment based on multiple tests [32]. In recent years, with the continuous development of optimization algorithms, many scholars have used them to optimize VMD parameters; they include the Genetic Algorithm (GA) [33], Grey Wolf Optimizer (GWO) [34], and Sparrow Search Algorithm (SSA) [35], etc. To better resist noise interference and make an adaptive selection of VMD parameters, an improved Sparrow Search Algorithm (SCSSA) is used to search for the optimal parameter combination for VMD with the smallest mode envelope entropy as the objective function. Therefore, an improved VMD decomposition model method based on SCSSA is proposed to effectively decompose settlement data sequences. Additionally, the decomposed sub-sequences have different levels of complexity, which will affect the prediction results. Sample entropy (SE) is used to measure the complexity of each sub-sequence [36].

In summary, due to diverse noise interferences and nonlinearity in mining subsidence monitoring data sequences, achieving high prediction accuracy is often challenging. This paper proposes a hybrid prediction model based on SCSSA-VMD-SE and ARIMA-BP by optimizing VMD parameters through the integration of sine and cosine with Cauchy variance in SCSSA to find the optimal decomposition. Firstly, SCSSA is utilized to optimize the VMD parameters, enabling the selection of the best VMD parameter combination. Secondly, based on the sample entropy of the sub-series derived from the decomposition of the original data, sequences exhibiting distinct characteristic trends and fluctuations are identified. Lastly, the ARIMA time series model is employed to predict trend sequences, while the backpropagation (BP) neural network model predicts fluctuation sequences. The predictions from both models are aggregated to yield the final settlement prediction result. Comparisons are made with a single prediction model, and the effectiveness and feasibility of the combined model are verified through an analysis of the prediction results obtained by processing GNSS monitoring data for the Banji mine.

2. Methodology

2.1. Variational Mode Decomposition

Variational mode decomposition (VMD) is a signal processing technique used to decompose complex raw data signals into a series of Intrinsic Mode Functions (IMFs) [37]. Through the optimization of a formulated problem, it adaptively decomposes the original subsidence data in the mining area and effectively extracts the main components and features of the signal, reducing the influence of nonlinearity and non-stationarity on the prediction results. Steps of the VMD algorithm: Firstly, perform the Hilbert transform on the original data to obtain various modal functions $\mu_k(t)$ and compute their one-sided spectra. Secondly, transform these spectra into a fundamental frequency band to estimate bandwidths and formulate the corresponding constrained variational problem. Finally, introduce Lagrange multipliers $\lambda(t)$ and the quadratic penalty factor α , converting it into an unconstrained variational problem. The specific formulas for the VMD algorithm are as follows:

$$L(\{\mu_k\}, \{\omega_k\}, \lambda) = \alpha \sum_k \left\| \partial_t \left[\left(\delta(t) + \frac{j}{\pi t} \right) * \mu_k(t) \right] e^{-j\omega_k t} \right\|_2^2 + \left\| f(t) - \sum_k \mu_k(t) \right\|_2^2 + \langle \lambda(t), f(t) - \sum_k \mu_k(t) \rangle \quad (1)$$

In Equation (1), μ_k represents the mode component, and ω_k represents the corresponding center frequency. Since setting different numbers of decomposition modes (k) and the quadratic penalty parameter (α) will affect the decomposition results, the selection of parameters k and α is crucial in VMD.

2.2. SCSSA

The Sparrow Search Algorithm (SSA) is an optimization algorithm that was designed by simulating the foraging and anti-predatory behavior of sparrows. It possesses several advantages, including high search accuracy, robust optimization capabilities, and ease of implementation. These qualities have led to its widespread application across various domains. Xue [38] provided a detailed introduction to the principles and the entire optimization process.

To address the issue of population diversity loss in the later stages of optimization with the SSA algorithm, leading to problems such as falling into local extremes and insufficient convergence accuracy [39].

In this paper, a reflection-based reverse-learning mechanism is utilized to initialize the sparrow population. N sparrow positions, $x_{i,j}$, are randomly initialized within the optimization range. The reflected reverse population is generated using Equation (2):

$$x_{i,j}^* = \frac{l_j + u_j}{2} + \frac{l_j + u_j}{2k} - \frac{x_{i,j}}{k} \tag{2}$$

In this formula, $x_{i,j}$ represents the position of the i -th sparrow in the j -th dimension ($i = 1, 2, \dots, d; j = 1, 2, \dots, N$), where d represents the population size, and N represents the dimensionality; $x_{i,j}^*$ represents the reflected reverse position; l_j and u_j are the minimum and maximum values of the search space in the j -th dimension; and k is the scaling factor. Based on the ascending order of the fitness values, we select the top N sparrow individuals as the initial population.

Due to the loss of population diversity caused by the stagnation of the entire population, followers often forage around the optimal discoverer, and the foraging process may involve competition for food, where followers attempt to become the new discoverers, thus increasing the possibility of falling into a local optimum. Therefore, the Sine Cosine Algorithm (SCA) is introduced to update the positions of the discoverers, as it can maintain the diversity of discoverer individuals, thus helping to enhance the global search capability of the Sparrow Search Algorithm [40]. The update to the discoverer's position $X_{i,j}^{t+1}$ is achieved through Equation (3):

$$\begin{cases} r_1 = a \times \left(1 - \left(\frac{t}{Iter_{max}}\right)^\eta\right)^{1/\eta} \\ \omega = \frac{e^{\frac{t}{Iter_{max}} - 1}}{e - 1} \\ X_{i,j}^{t+1} = \begin{cases} \omega \times X_{i,j}^t + r_1 \times \sin r_2 \times \left|r_3 \times X_{best} - X_{i,j}^t\right|, R < ST \\ \omega \times X_{i,j}^t + r_1 \times \sin r_2 \times \left|r_3 \times X_{best} - X_{i,j}^t\right|, R \geq ST \end{cases} \end{cases} \tag{3}$$

In Equation (3), r_1 represents the linearly decreasing search factor; $a = 1$; $Iter_{max}$ is the maximum number of iterations; t is the iteration count; η is the adjustment factor, $\eta \geq 2$; ω is the nonlinear weighting factor; X_{best} is the current overall best position; r_2, r_3 are random numbers in the range $[0, 2\pi]$, determining the sparrow's movement distance and controlling the influence of the best individual on the sparrow's subsequent position; and $R \in [0, 1]$ and $ST \in [0.5, 1]$ represent vigilance and safety values, respectively.

Then, the Cauchy mutation strategy is introduced to enhance global optimization capability. The update to the follower's position is carried out according to Equation (4):

$$X_{i,j}^{t+1} = X_{best}(t) + cauchy(0,1) \oplus X_{i,j}(t) \tag{4}$$

In Equation (4), $cauchy(0,1)$ represents the standard Cauchy distribution function, and " \oplus " denotes element-wise multiplication.

Finally, we determine whether the current iteration count meets the termination condition. If the condition is satisfied, we output the optimal fitness value and the best position [41].

2.3. SCSSA-VMD

The selection of VMD parameters affects the decomposition results, and the number of decomposition modes (k) and the quadratic penalty parameter (α) have a significant impact on the decomposition results. Therefore, studying the optimal values for k and α is crucial. Empirical values are typically used for other parameters [42].

Information entropy can be used to assess the sparsity of a signal, and the value of information entropy also reflects the uncertainty of the signal. A higher entropy value indicates greater uncertainty in the signal. The entropy value of the decomposed sub-sequence e_j is the envelope entropy, which can reflect the sparsity characteristics of the original signal. The envelope entropy E_e of the signal $x(j)$ can be expressed as:

$$\begin{cases} E_e = -\sum_{j=1}^N e_j \lg e_j \\ e_j = a(j) / \sum_{j=1}^N a(j) \end{cases} \quad (5)$$

In Equation (5), e_j represents the normalized form of $a(j)$, and $a(j)$ represents the envelope information of the signal $x(j)$ after the Hilbert transform.

In order to search for the global optimum (k, α), the entire optimization process utilizes the local minimum envelope entropy value as the fitness value and minimizes the local minimum envelope entropy value as the final parameter optimization goal. The SCSSA algorithm is used to adaptively optimize VMD and determine the best two preset parameters (k, α) for VMD. The specific process of the SCSSA-VMD method is as follows:

- (1) Initialize the specific parameters for SSA and VMD;
- (2) Utilize a refracted backpropagation learning mechanism to initialize the sparrow population, decompose the original subsidence data using VMD, and use envelope entropy as the fitness function for global search.
- (3) Update the discoverer's positions of the original Sparrow Algorithm using the Sine Cosine Strategy, improve the step-size search factor for the Sine Cosine Strategy, and update the follower's positions of the original Sparrow Algorithm using the Cauchy mutation strategy.
- (4) Following steps 2 to 3, when the envelope entropy value reaches the minimum, obtain the current best two parameters (k, α) for VMD. Utilize these optimal parameters to perform VMD decomposition on the original subsidence data.

2.4. Sample Entropy

Sample entropy (SE) is a statistical measure used to analyze time series data, describing the complexity and irregularity of the data. It can be utilized to detect regularity or periodicity in time series data. Higher values of sample entropy indicate higher irregularity and complexity in the time series data, potentially indicating noise or randomness. Conversely, lower values indicate higher regularity in the time series data, suggesting periodicity or pattern regularity. It can be expressed using a pseudo-mathematical expression as follows [43]:

$$SE = E(w, m, r) \quad (6)$$

In Equation (6), w represents the time series, and m is the embedding dimension. The similarity tolerance r is set to 0.2 times the standard deviation (std) of the time series.

3. Prediction Model

3.1. ARIMA Model

In the equation, e_j represents the normalized form of $a(j)$, and $a(j)$ represents the envelope information of the signal $x(j)$ after Hilbert transform. The ARIMA model is

a classical time series analysis method used for modeling and forecasting stationary or non-stationary time series [44]. It is a simple yet effective method that is widely utilized in practical applications. The ARIMA model is a statistical method based on time series data, treating the fluctuation of data over time as a random sequence and attempting to characterize and describe the regularities of this random sequence using a mathematical model. In the modeling process, the model is mainly controlled using three parameters, p , d , and q , where p represents the number of autoregressive terms, q represents the number of moving average terms, and d represents the order of differencing. The structure of the ARIMA(p, d, q) model is as follows:

$$\begin{cases} (1 - \phi_1 B - \phi_2 B^2 - \dots - \phi_p B^p) \nabla^d x_t = (1 - \theta_1 B - \theta_2 B^2 - \dots - \theta_q B^q) \delta_t \\ E(\delta_t) = 0, \text{Var}(\delta_t) = \sigma_\varepsilon^2, E(\delta_t \delta_s) = 0, s \neq t \end{cases} \quad (7)$$

In Equation (7), x_t is the system signal, δ_t is the model error, B is the lag operator, d is the differencing operator, ϕ_p is the autoregressive coefficient, and θ_q is the moving average coefficient.

3.2. BP Model

The BP neural network is a multi-layer feedforward neural network based on the error backpropagation algorithm. It is one of the most successful and widely used neural network models. The BP neural network approximates the desired output by continuously adjusting the network's weights and thresholds. During the training process, input samples are forwarded through the network to the output layer. The error between the actual output and the expected output is calculated, and this error is then used to adjust the network parameters in a backward fashion [29]. The structure of a BP neural network consists of an input layer, hidden layers, and an output layer. The BP neural network structure is illustrated in Figure 1 below:

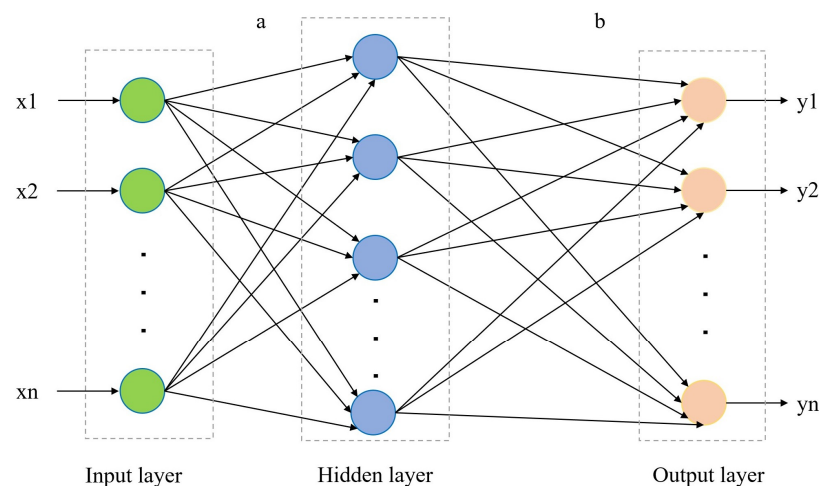


Figure 1. The structure of a BP neural network.

x_1, x_2, \dots, x_n are input values; a represents the weights between the input layer and the hidden layer; b represents the weights between the hidden layer and the output layer; and y_1, y_2, \dots, y_m are the output results. The initial number of nodes in the hidden layer is obtained through an empirical formula, as follows:

$$h = \sqrt{n + m} + c \quad (8)$$

In Equation (8), h represents the number of nodes in the hidden layer, n represents the number of nodes in the input layer, m represents the number of nodes in the output layer, and c is a random positive integer, typically less than 10.

3.3. SCSSA-VMD-SE and ARIMA-BP Model

The combined SCSSA-VMD-SE and ARIMA-BP model is shown in Figure 2. The modeling steps for the entire process are as follows:

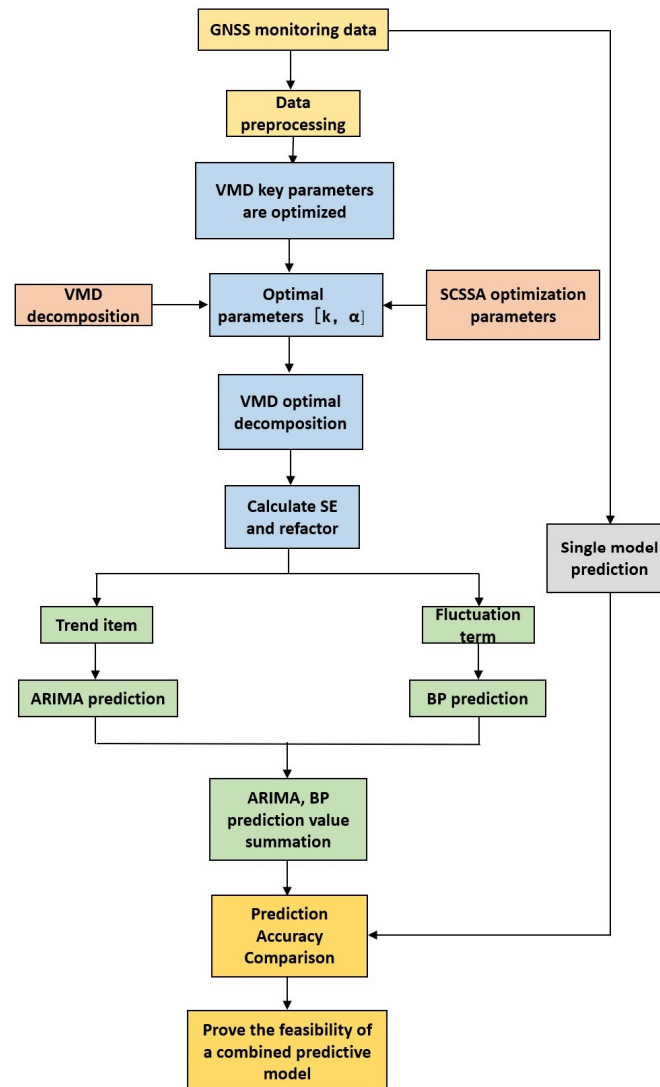


Figure 2. The prediction flow chart.

The combined subsidence prediction model proposed in this paper encompasses four fundamental steps:

Step 1: Preprocess the original monitoring data by removing outliers. Due to debugging issues, such as equipment calibration and platform upgrades during long-term monitoring, short-term data interruptions occur. Cubic spline interpolation can be employed to provide a smoother curve and is less likely to cause Runge's phenomenon compared to other interpolation methods [45]. Therefore, use cubic spline interpolation to complete the missing values in the original data.

Step 2: Utilize SCSSA for adaptive parameter optimization of VMD. Subsequently, apply the optimized VMD to decompose the original data, resulting in various mode components.

Step 3: Calculate the sample entropy values for each mode component and reconstruct the decomposed data into trend and fluctuation components.

Step 4: Use the ARIMA model and BP neural network model, respectively, to predict the trend and fluctuation components. Sum up the predictions for each component to obtain the final prediction result.

4. Engineering Overview

Banji Coal Mine is situated at the border of Lixin County and Yingshang County, extending approximately 5.3 km in an east–west direction and about 2.5 to 6.7 km in a north–south direction, covering an area of roughly 30 square kilometers. The designed annual production capacity of Banji Coal Mine is one million tons of high-quality thermal coal, with a planned service life of 53 years. The mining operation for the 110801 initial mining face was scheduled to commence in April 2021. Banji Coal Mine adopts a single-wing mining approach, situating the entire mining area to the west of the industrial square. The loose layer spans approximately 542 to 713 m in thickness, and the bottom of the loose layer contains a water-bearing layer directly overlying the coal-bearing strata. To monitor the mining impact on the 110801 initial mining face, surface movement and deformation are monitored. Real-time dynamic GNSS monitoring is conducted in significant affected areas. A monitoring network for surface movement and deformation is established to promptly collect data and create theoretical prediction models. This aids in anticipating potential impacts on structures within the industrial square, including mine shafts, well frames, and loading warehouses, during the mining process, and proposing safety measures in a timely manner. Technical support is also provided for coal pillar retention design and subsidence prediction for the mine through the establishment of a GNSS real-time dynamic monitoring system. The GNSS real-time dynamic monitoring system comprises one reference station and eight real-time monitoring stations. The reference station is positioned on the roof of the industrial square office building. During the 110801 mining face’s extraction period, four real-time monitoring stations are situated in crucial areas affected by the 110801 mining face. The reference station BJCMP is installed on the rooftop of the Banji Coal Mine office building, composed of stainless steel. For the 110801 mining face, four real-time monitoring stations are installed. One of the real-time monitoring stations is placed at the intersection of the trend observation line and the dip observation line of the 110801 mining face (MCORS02). The setup of the BJCMP reference station and GNSS monitoring station equipment is depicted in Figure 3. The location marked within the red box represents the BJCMP reference station. The Chinese letters in the figure signify “Banji Coal Mine”. Three real-time monitoring stations (MCORS06, MCORS07, MCORS08) are located in vital areas along the trend observation line, toward the factory square, and in the middle of the 110801 mining face, as indicated in the GNSS monitoring station setup diagram in Figure 4.

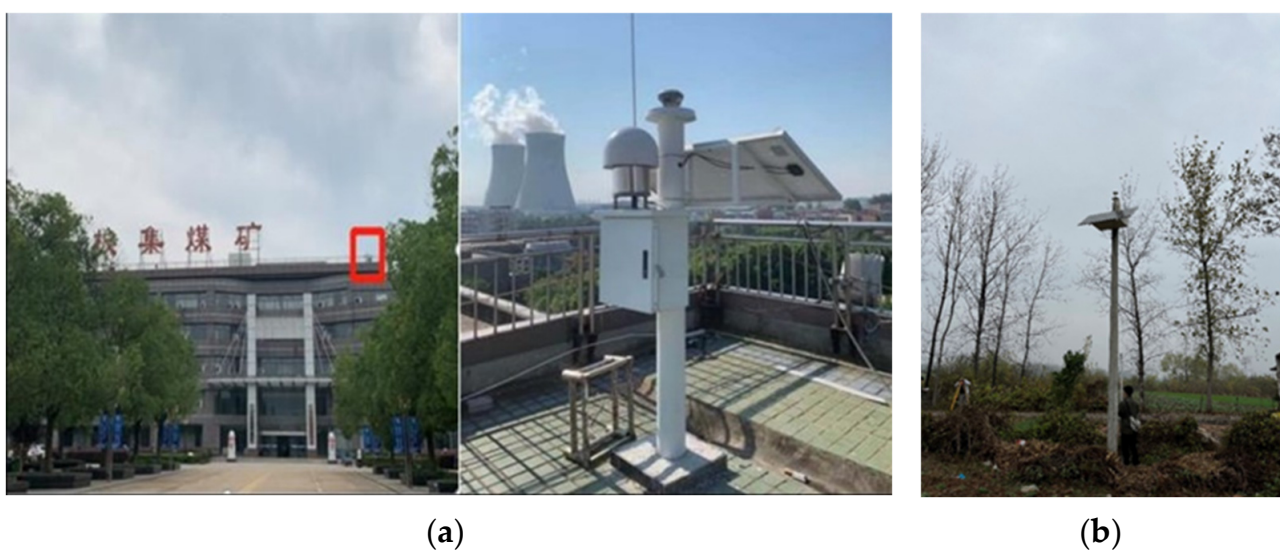


Figure 3. The surroundings of the reference station and monitoring stations: (a) the surroundings of the BJCMP reference station site; (b) the surroundings of the MCORS02 monitoring station site.

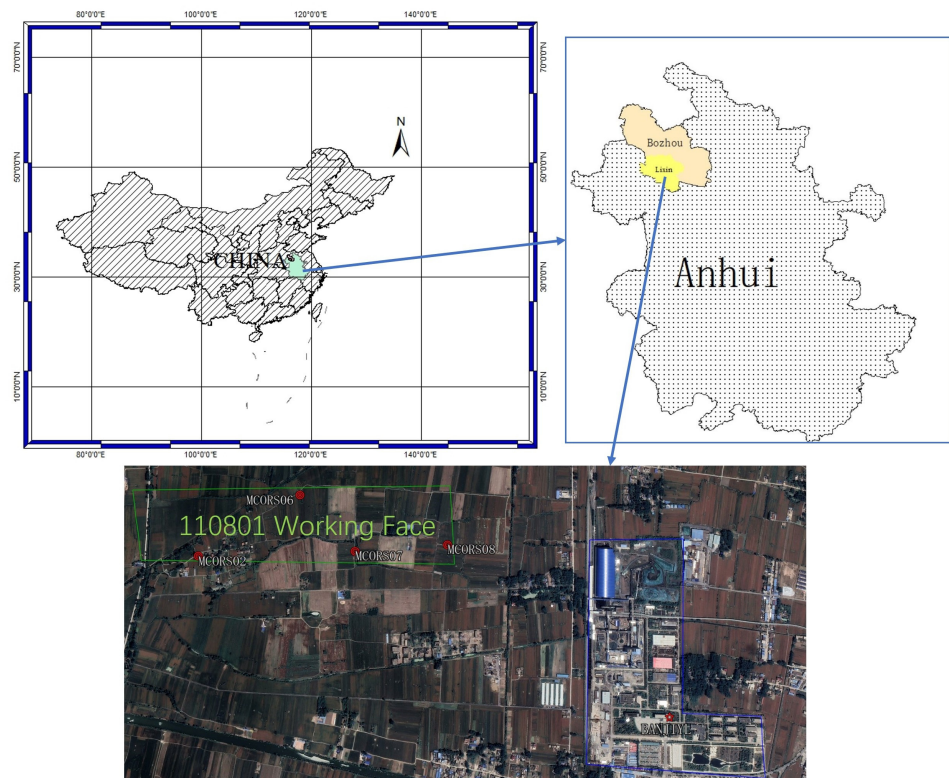


Figure 4. Schematic diagram of monitoring stations in the study area.

The surface deformation monitoring stations utilize independently designed and assembled BeiDou displacement monitoring devices (E-8s) for data collection. The specific receiver parameters are indicated in Table 1.

Table 1. E-8s displacement monitoring device main parameters.

| Real-Time Dynamic Plane Accuracy | Real-Time Dynamic Vertical Accuracy | Static Differential Horizontal Accuracy | Static Differential Vertical Accuracy | Power | Data Transmission |
|----------------------------------|-------------------------------------|---|---------------------------------------|-------|---|
| 8 mm + 1 ppm | 15 mm + 1 ppm | 2.5 mm + 1 ppm | 5 mm + 1 ppm | 2–6 W | Built-in 4G SIM card communication module |

5. Engineering Case Analysis

5.1. Subsection

This study utilized elevation component monitoring data from four GNSS monitoring stations at the 110801 working face of Banji Coal Mine as experimental data. The observation period extended from 13 July to 22 September 2021, totaling 72 days. Observations were conducted at 6 h intervals, resulting in 288 sets of experimental data for the elevation component. The last eight sets of monitoring data were used for prediction, spanning a total of two days. The continuous settlement data exhibited notable deviations in some individual points due to factors such as equipment and the surrounding environment. Values that did not conform to the anticipated settlement patterns were manually removed, and missing data were addressed through cubic spline interpolation during preprocessing. The settlement data for each monitoring station, presented in Figure 5, illustrate the impact of these steps. As mining progresses from west to east, the monitoring stations are labeled accordingly: MCORS02, MCORS06, MCORS07, and MCORS08. Notably, MCORS02 demonstrates the highest settlement magnitude and relatively stable settlement. Conversely, MCORS06 and MCORS07 exhibit more fluctuation in their settlement data, albeit generally following the descending trend associated with mining subsidence. MCORS08, being further from the mining point, experiences relatively intense fluctuations. Over a

shorter timeframe, it undergoes less settlement, displaying a comparatively stable settlement pattern. In summary, the settlement values at each monitoring station align with the surface settlement patterns in the mining area. Proximity to the mining point correlates with larger and more stable settlement values, whereas stations further from the mining point experience less settlement and demonstrate greater fluctuations.

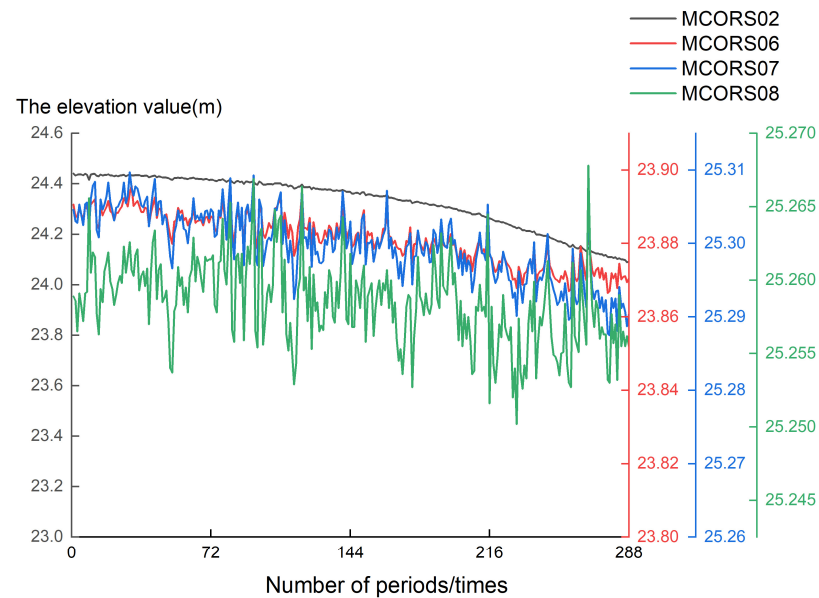


Figure 5. Settlement variation graphs for each monitoring station.

The experimental hardware setup includes an i7-12700F CPU, 32 GB RAM, Nvidia GTX 2060, and a Windows 10 operating system. All models run on MATLAB R2022a.

By analyzing the subsidence monitoring data of the maximum subsidence point MCORS02 and monitoring stations MCORS06, MCORS07, and MCORS08 in the important area towards the factory square in the middle of the 110801 working face, this study demonstrates the establishment of the combined model based on SCSSA-VMD-SE and ARIMA-BP.

5.2. VMD Result Analysis

5.2.1. Optimization Result of VMD Using SCSSA

To demonstrate the effectiveness of the SCSSA algorithm, four test functions were selected for simulation analysis. The test functions are shown in Table 2. Additionally, to demonstrate the optimization ability of the SCSSA algorithm, comparisons were made with SSA, GWO, and PSO. The population size was set to 30, the maximum number of iterations was set to 500, and the dimensionality was set to 30. The specific parameters for each algorithm are shown in Table 3. These four test functions all have a certain level of difficulty in solving, making them suitable for testing the optimization performance of the algorithm. The convergence curves for each algorithm for the four functions are shown in Figure 6. For each test function, SCSSA consistently demonstrated a better convergence speed compared to other optimization algorithms. From the figures, it can be seen that for each test function, the SCSSA algorithm consistently demonstrates better convergence speed than the other optimization algorithms. Moreover, it is capable of escaping local optima and finding the global optimum. The SCSSA algorithm exhibits higher stability and faster convergence speed. In summary, the proposed SCSSA optimization algorithm exhibits faster convergence speed and stronger global search capabilities, giving it a significant advantage in optimization performance. Compared to the other three optimization algorithms, SCSSA consistently demonstrates superior optimization performance.

Table 2. Benchmark test functions.

| Function | Dim | Range |
|---|-----|-------------|
| $F_1 = \sum_{i=1}^n x_i + \prod_{i=1}^n x_i $ | 30 | [-10, 10] |
| $F_2 = \max_i \{ x_i , 1 \leq i \leq n\}$ | 30 | [-100, 100] |
| $F_3 = -20 \exp\left(-0.2 \sqrt{\frac{1}{n} \sum_{i=1}^n x_i^2}\right) - \exp\left(\frac{1}{n} \sum_{i=1}^n \cos(2\pi x_i)\right) + 20 + e$ | 30 | [-32, 32] |
| $F_4 = \sum_{i=1}^n -x_i \sin \sqrt{ x_i }$ | 30 | [-500, 500] |

Table 3. Parameter settings of the optimization algorithm.

| Algorithm | Parameter Settings |
|-----------|---|
| PSO | The inertia weight w is 0.8, learning factor $c1 = c2 = 1.5$, $r1$ and $r2$ are random values between 0 and 1. |
| GWO | The convergence factor $a = 2 - t \times (2/\text{iter}_{\max})$, $r1$ and $r2$ are random values between 0 and 1. |
| SSA | Same as the ISSA algorithm. |

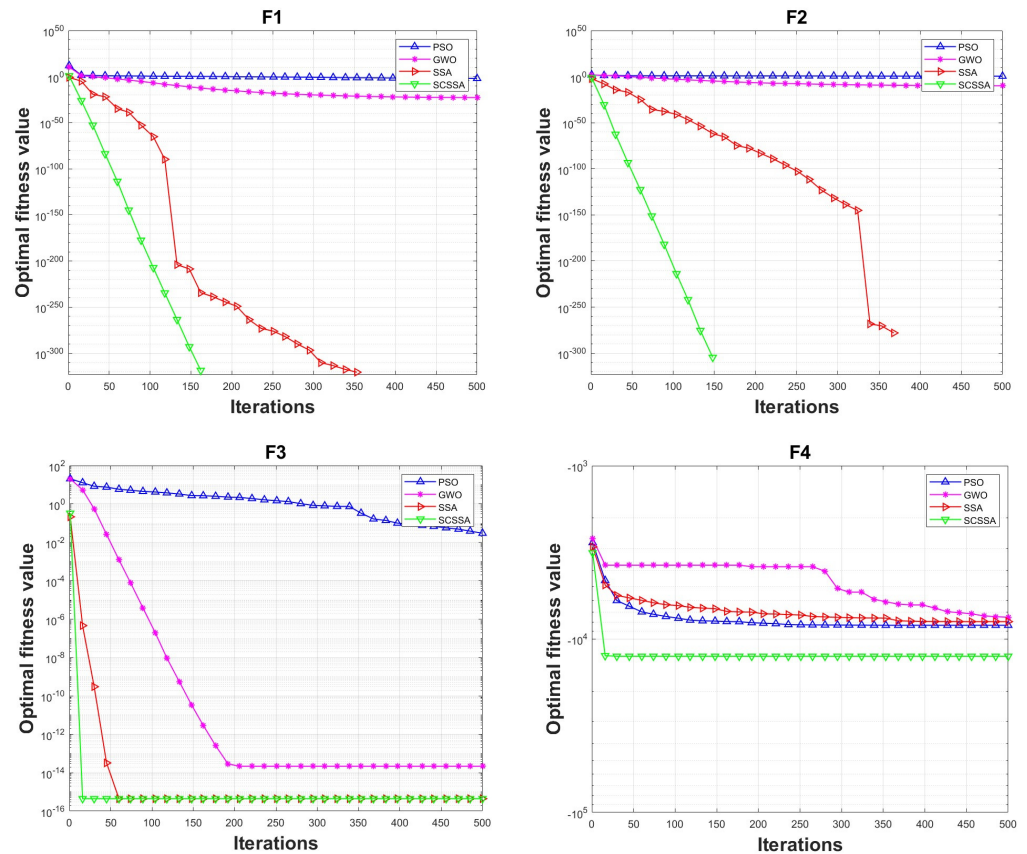


Figure 6. Comparison of convergence curves of each optimization algorithm.

5.2.2. Decomposition of Settlement Data Using SCSSA-VMD

To obtain the optimal parameter combination (k, α) for VMD, SCSSA was used to acquire the best parameters for VMD. The SCSSA-VMD parameter settings are shown in Table 4, and Figure 7 depicts the iteration process for optimizing VMD parameters using SCSSA and SSA for the data from the four CORS monitoring stations. In contrast to SSA, the SCSSA curve not only consistently maintains its position at the bottom, but also showcases robust and efficient optimization capabilities, demonstrating rapid convergence. This distinguishing feature highlights the effectiveness of SCSSA in enhancing

the performance and convergence speed of the optimization process when compared to traditional SSA methods.

Table 4. Parameter settings for SCSSA-VMD.

| Populations | Number of Iterations | Value Range of K | Value Range of α |
|-------------|----------------------|------------------|-------------------------|
| 20 | 50 | [1, 15] | [100, 2500] |

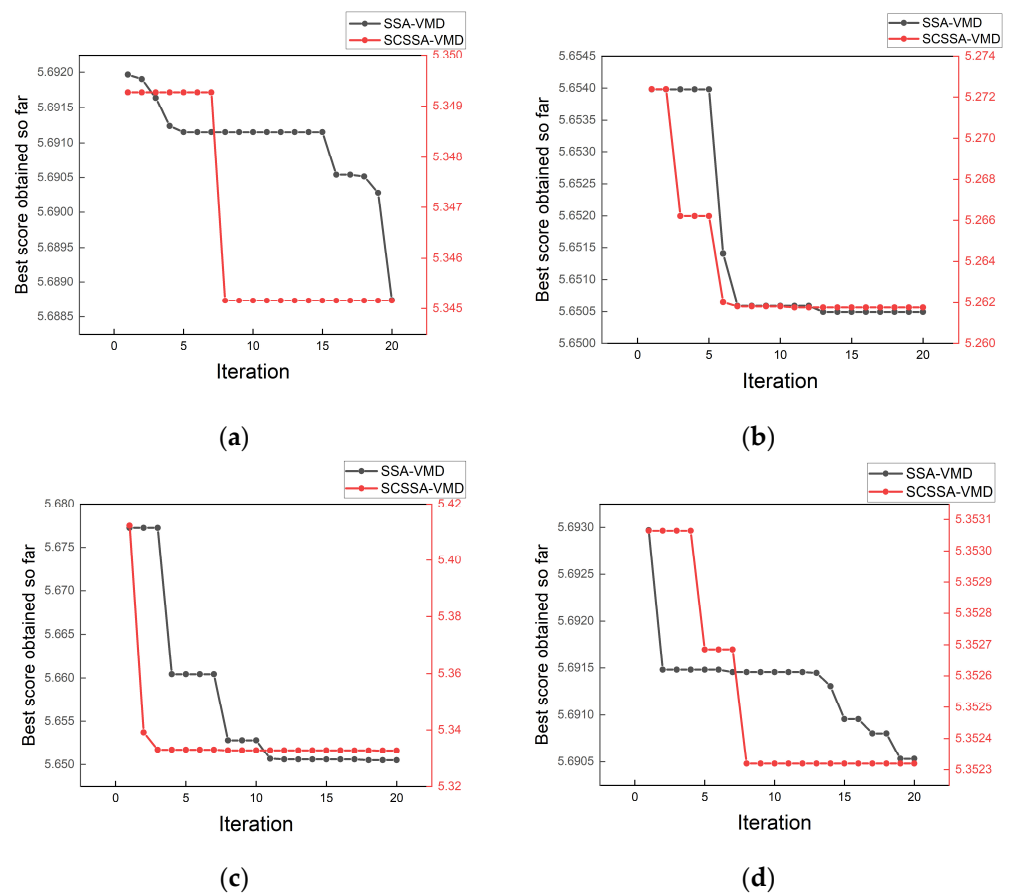


Figure 7. Comparison of convergence curves of each optimization algorithm: (a) MCORS02; (b) MCORS06; (c) MCORS07; (d) MCORS08.

The final parameters for SCSSA-optimized VMD for the four monitoring stations' data are presented in Table 5.

Table 5. The VMD parameters generated by SCSSA for each monitoring station.

| Datasets | Parameters | |
|----------|------------|----------|
| | k | α |
| MCORS02 | 13 | 201 |
| MCORS06 | 15 | 2368 |
| MCORS07 | 15 | 1909 |
| MCORS08 | 15 | 2466 |

The original elevation series and decomposed Intrinsic Mode Functions (IMFs) of subsidence data from each CORS monitoring station are shown in Figure 8. Each plot, from top to bottom, represents IMF1 to IMF n . It can be seen from the figures that the sub-sequences decomposed by SCSSA-VMD are more stable and regular, which helps to improve the predictability of the time series.

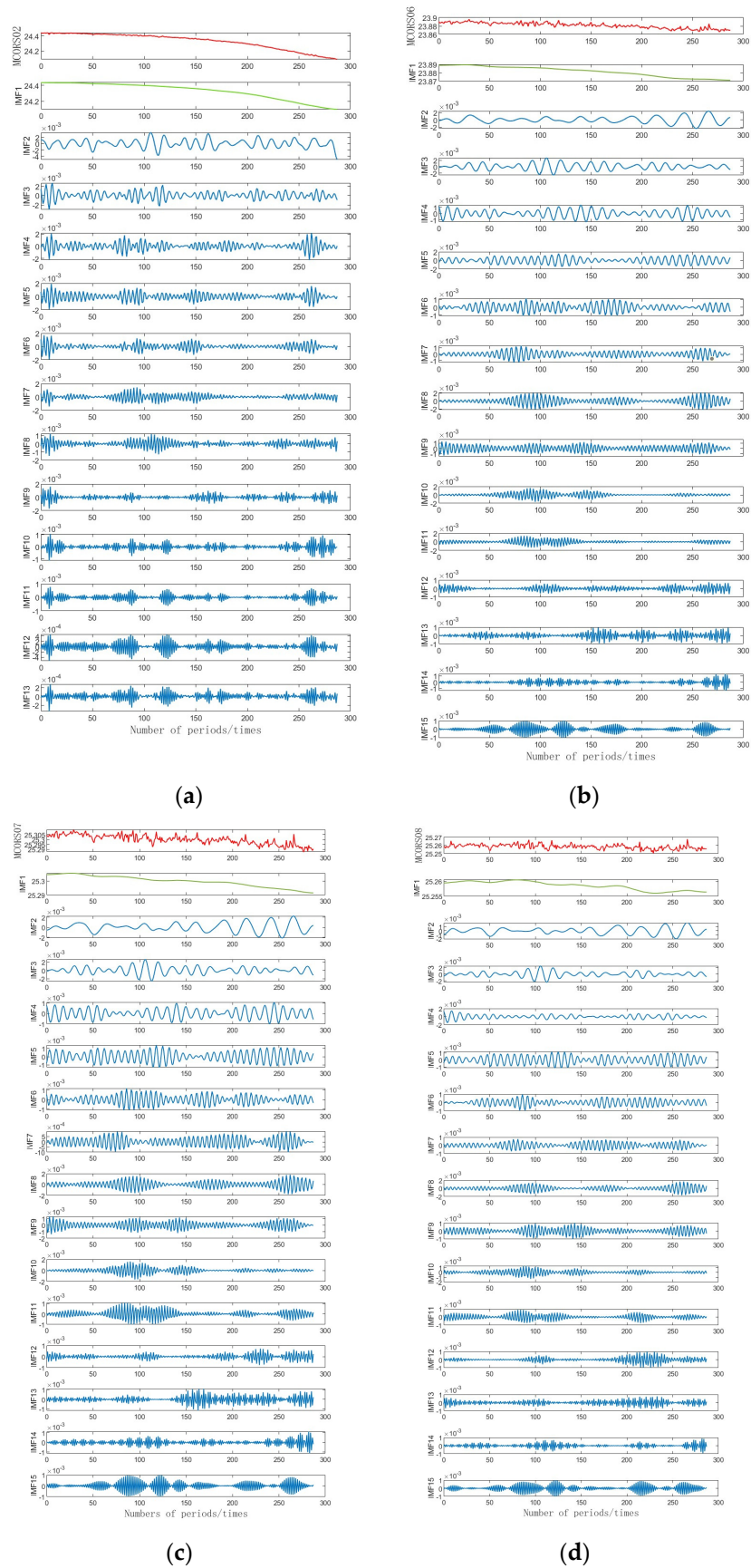


Figure 8. The SCSSA-VMD decomposition results for the MCORS02 monitoring station: (a) MCORS02; (b) MCORS06; (c) MCORS07; (d) MCORS08.

5.3. VMD Result Analysis

SCSSA-VMD decomposes a finite number of IMF components with different complexities. Utilizing appropriate models for sub-sequences with different complexities helps to leverage the capabilities of the models and improve prediction performance. The sample entropy parameter settings were as follows: embedding dimension for phase space reconstruction, $\text{dim} = 2$, and delay time, $\tau = +1$. Figure 9 shows the sample entropy values of each IMF after decomposition for the four CORS monitoring stations. From Figure 9, it can be seen that the sample entropy value of IMF1 is the smallest. Through multiple experiments, different values were selected from $[0.1, 0.2, \dots, 0.5, 0.6]$ to determine the SE threshold. Through multiple experiments, the SE threshold was set to 0.1, where the fluctuation component is below 0.1 and the high-frequency component is above 0.1. Reconstruction was carried out based on the SE values, where the first component of the four datasets represents the trend component, while the rest represent the fluctuation components. The reconstruction results are shown in Figure 10.

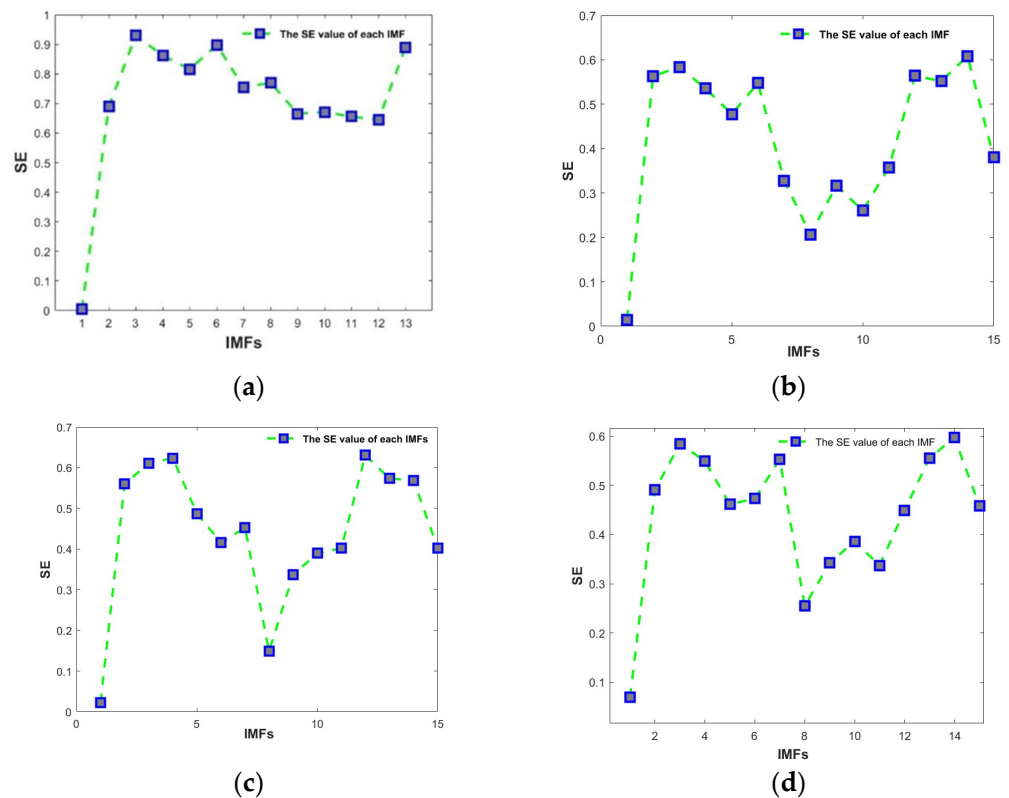


Figure 9. The sample entropy values of IMF for each monitoring station: (a) MCORS02; (b) MCORS06; (c) MCORS07; (d) MCORS08.

5.4. The Combined Model Prediction

Through the analysis of subsidence data from the MCORS02 monitoring station, the establishment of the SCSSA-VMD-SE-ARIMA-BP hybrid model is explained, with the specific process shown in Figure 11.

5.4.1. Trend Component Prediction

The trend component sequence was predicted using the ARIMA model. First, an Augmented Dickey–Fuller (ADF) test was conducted on the data to assess their stationarity. Since differencing can result in data loss, d is generally set to 1 or 2 to avoid the loss of data. Then, the values of p and q in the ARIMA model were determined by calculating the Akaike Information Criterion (AIC). An exhaustive search method was used, and the best forecasting performance was achieved when p was set to 2 and q to 4. Figure 12 shows

that the modeling results have a good fit with the subsidence data trend component during the training process, demonstrating the model's ability to predict the trend component sequence effectively.

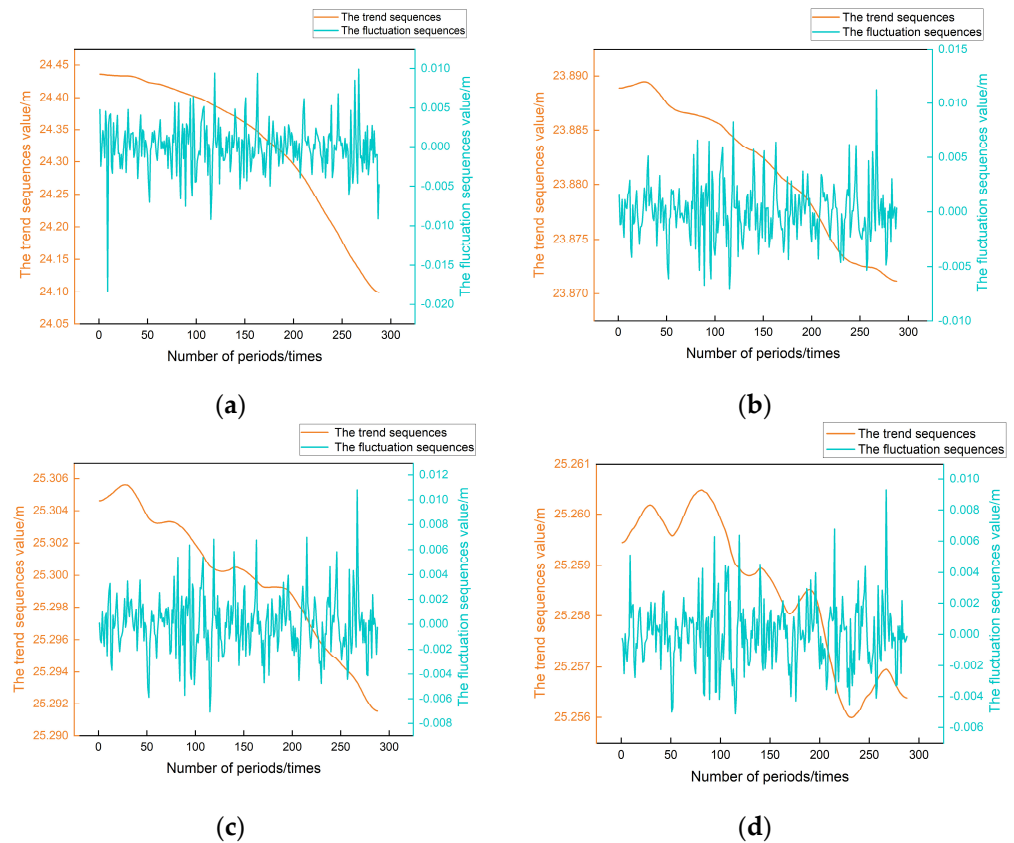


Figure 10. The reconstruction results for each monitoring station: (a) MCORS02; (b) MCORS06; (c) MCORS07; (d) MCORS08.

5.4.2. Fluctuation Component Prediction

The BP neural network model was utilized to predict the fluctuation component sequence. The advantages of the Levenberg–Marquardt algorithm's good local optimization effect are used for precise solving in a small range, thereby improving the neural network's convergence speed, accuracy, and prediction precision [46]. The network is configured with a maximum training limit of 1000 iterations, a target error of 0.00001, and a learning rate of 0.01. The tansig function is chosen as the transfer function from the input layer to the hidden layer, while the purelin function serves as the transfer function from the hidden layer to the output layer. The network's training accuracy and convergence speed and the number of hidden layer nodes have a significant relationship. The number of nodes is commonly selected using empirical Formula (8). After multiple adjustments, it is found that the network performs best when $h = 3$; therefore, three hidden layer nodes are chosen. Figure 13 demonstrates the results of using the BP neural network to predict the fluctuation component sequence.

5.4.3. Accumulated Subsidence Prediction

The predicted results of the trend component and the fluctuation component were added to obtain the cumulative subsidence prediction result, as shown in Figure 14.

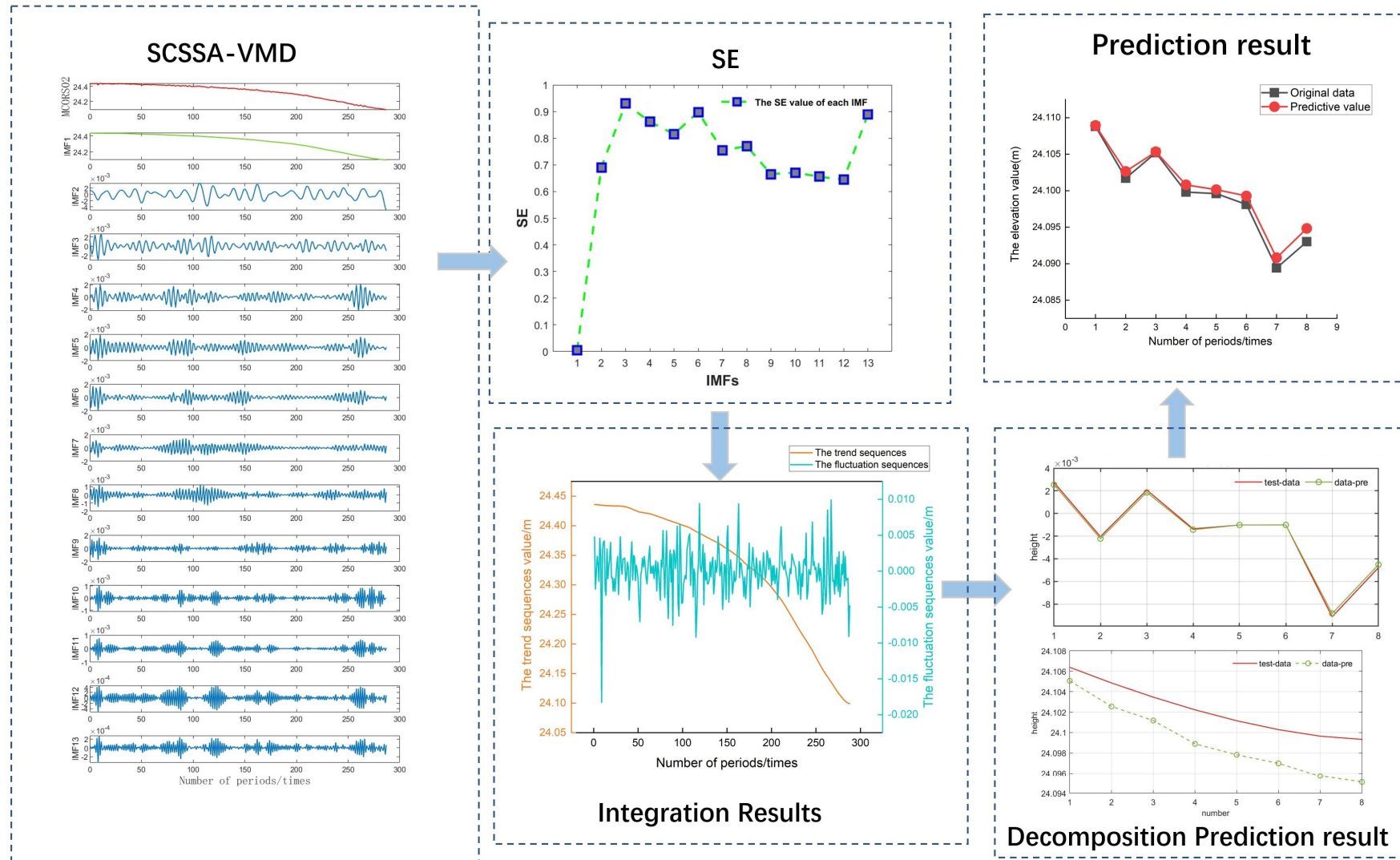


Figure 11. Model prediction process for the MCORS02 monitoring station.

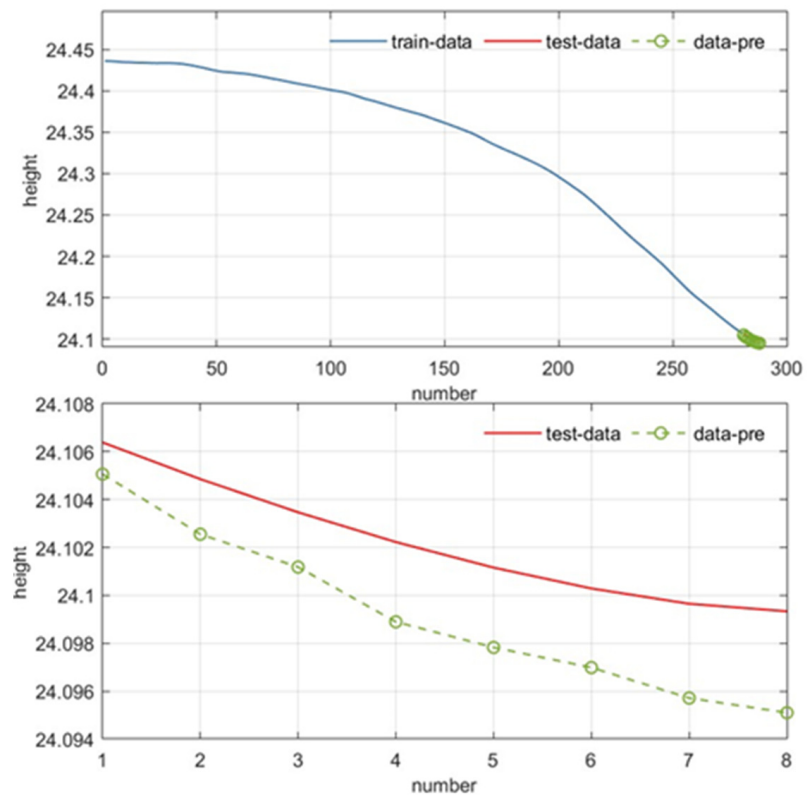


Figure 12. The prediction results for the trend component.

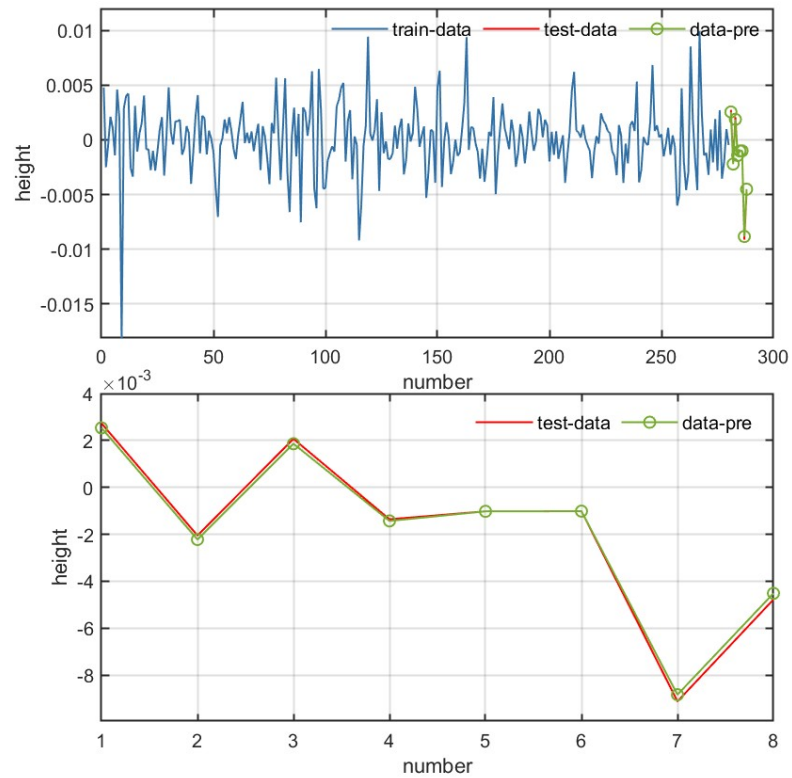


Figure 13. The prediction results for the fluctuation component.

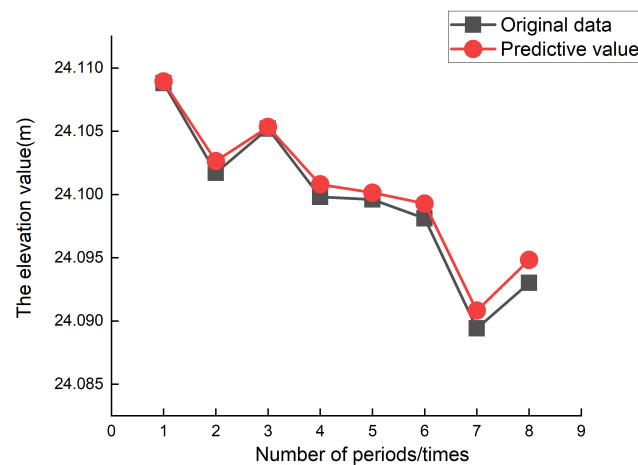


Figure 14. The prediction results for the MCORS02 monitoring station.

6. Discussion

The predictive capabilities of the proposed SCSSA-VMD-SE and ARIMA-BP hybrid models were compared with the single prediction models BP and ARIMA. During the experiment, the SCSSA-VMD-BP and SCSSA-VMD-ARIMA models were constructed. The data were not segregated into trend and fluctuation components based on the value of SE; instead, each decomposed subsequence was separately predicted using BP and ARIMA. Diverse preprocessing techniques with various optimization algorithms were utilized to construct the SSA-VMD-SE and ARIMA-BP hybrid models for comparison. The final predictive results of each model and the actual subsidence data sequences at the four monitoring stations are presented in Figures 15–18. Observing the figures, it becomes evident that the single models, ARIMA and BP, exhibited poor prediction performance. The introduction of SCSSA-VMD for decomposing the original subsidence data sequences led to notable improvements in the prediction performance of the single models. Furthermore, decomposing the data using the optimized VMD into trend and fluctuation components for separate prediction demonstrated promising results. SCSSA-VMD exhibited superior performance compared to SSA-VMD in preprocessing the data, aligning well with the prediction trend. This validation supports that the proposed SCSSA-VMD-SE-ARIMA-BP hybrid model provides superior prediction results encompassing both the overall trend and detailed information compared to other models.

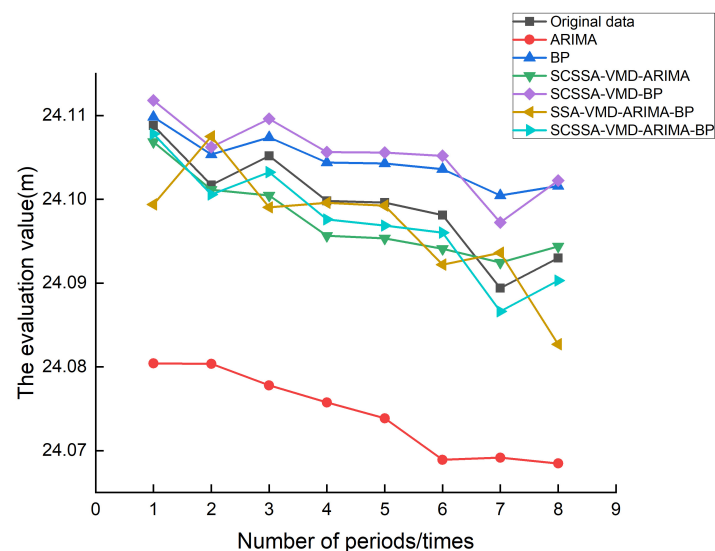


Figure 15. Comparison of prediction results for the MCORS02 monitoring station.

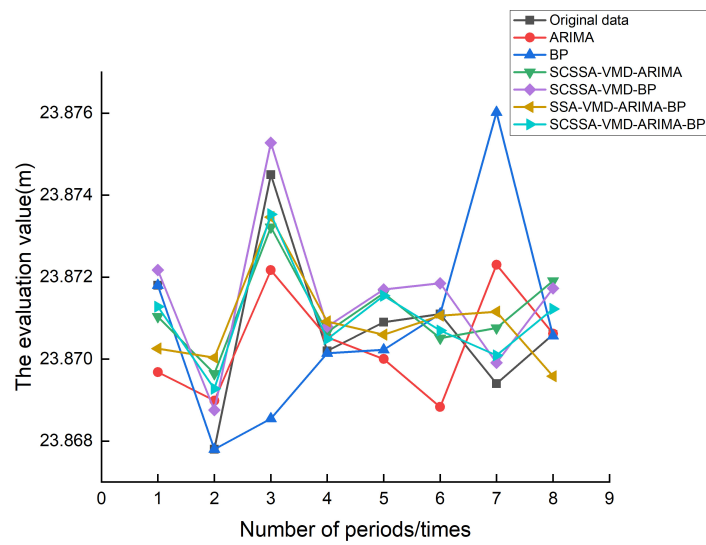


Figure 16. Comparison of prediction results for the MCORS06 monitoring station.

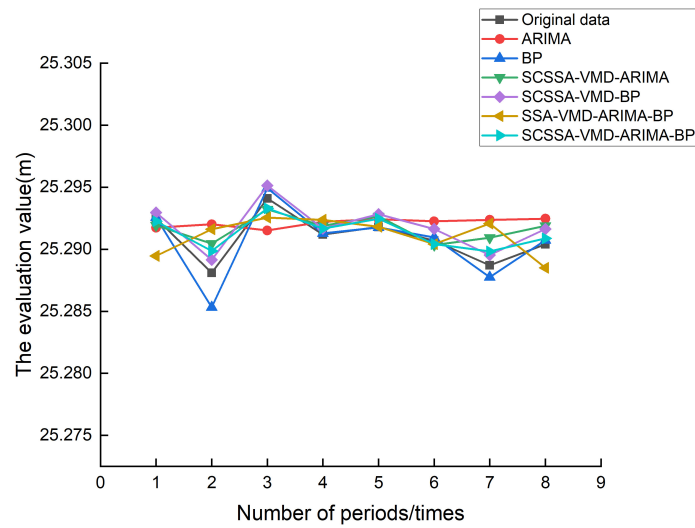


Figure 17. Comparison of prediction results for the MCORS07 monitoring station.

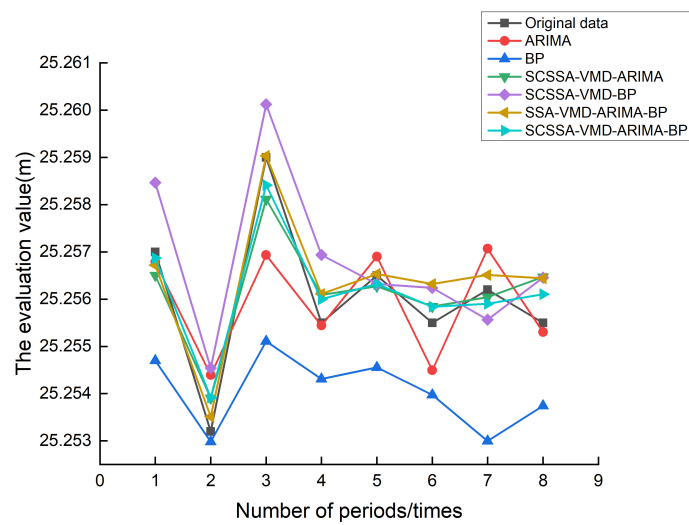


Figure 18. Comparison of prediction results for the MCORS08 monitoring station.

To accurately and objectively assess the predictive performance of the prediction model, this paper employed the root mean square error (RMSE), mean absolute error (MAE), and mean absolute percentage error (MAPE), with the respective formulas calculated as follows:

$$RMSE = \sqrt{\frac{1}{n} \sum_{i=1}^n (y_i - \hat{y}_i)^2} \quad (9)$$

$$MAE = \frac{1}{n} \sum_{i=1}^n (y_i - \hat{y}_i)^2 \quad (10)$$

$$MAPE = \frac{1}{n} \sum_{i=1}^n |y_i - \hat{y}_i| \quad (11)$$

A comprehensive statistical analysis of the prediction results for the four GNSS monitoring stations was conducted to thoroughly evaluate the prediction results of each model. The prediction accuracy for the four monitoring stations is presented in Table 6, and we interpret the data in the table as follows: For the MCORS02 monitoring station, being the closest to the mining subsidence point, it is most significantly affected by mining subsidence. The prediction accuracy of the single models is generally lower compared to the SCSSA-VMD-ARIMA-BP hybrid model proposed in this paper, and some turning points have poor prediction accuracy. For MCORS06, MCORS07, and MCORS08, which are relatively further from the mining subsidence point and less affected by mining subsidence, the SCSSA-VMD-ARIMA-BP hybrid model still exhibits the best prediction accuracy compared to the other models. Introducing VMD for data preprocessing effectively reduces data noise and modeling difficulty, enhances the richness of the original data, and improves prediction accuracy. When optimizing VMD using different optimization algorithms, SCSSA-VMD is more effective in decomposing data and extracting valuable information from subsidence data. The prediction accuracy is further improved for each monitoring station. MCORS08, being the furthest from the mining subsidence point, exhibits less significant subsidence data changes, resulting in a relatively smaller improvement in prediction accuracy when comparing SCSSA-VMD to SSA-VMD.

In conclusion, the prediction accuracy of traditional single models is much lower than that of combined models. The combined model can combine the advantages of each model and reduce the impact of the randomness and volatility of the settlement data sequence on the prediction by capturing changes in historical data in certain programming. Mining settlement is a complex process, and the settlement of key points is monitored, which can provide better early warning. Due to the lack of coal mine-related parameters, the prediction of surface subsidence can only be made through the elevation change data collected by the GNSS monitoring station set up in the 110801 working face of the mining area. Therefore, better prediction results were obtained by combining the splitting method with the combined model method. The splitting method first splits the original data into a small amount and uses different prediction methods to predict the small amount, thereby improving the prediction accuracy. By comparing the prediction data of various monitoring stations, the model proposed in this article has greatly improved prediction accuracy.

However, this study has certain limitations. While the proposed model demonstrates good prediction accuracy, the model's training demands are substantial, requiring a large dataset, and its generalizability remains limited. In future research, model parameters can be determined by introducing sensitivity analysis and using methods such as weight sharing to improve the prediction accuracy of the model [47,48]. Furthermore, this paper primarily focuses on the deformation information related to surface subsidence in the mining area. Consequently, the modeling process exclusively undertakes prediction and analysis for elevation data, omitting a specific examination of three-dimensional surface deformation. To enhance predictive accuracy, it would be beneficial to incorporate additional parameters such as coal mine geology, rock characteristics, hydrogeology, development methods, and other relevant factors during the prediction process [49]. Further

in-depth exploration and research are needed in future studies to reconstruct and model three-dimensional data [50].

Table 6. Model error values of each site.

| Site | Model | RMSE (mm) | MSE (mm) | MAE (mm) |
|---------|--------------------|-----------|-----------|----------|
| MCORS02 | ARIMA | 25.2937 | 0.063977 | 25.1135 |
| | BP | 6.0569 | 0.003607 | 5.1651 |
| | SCSSA-VMD-ARIMA | 3.4066 | 0.001116 | 3.0128 |
| | SCSSA-VMD-BP | 6.8467 | 0.003950 | 5.9933 |
| | SSA-VMD-ARIMA-BP | 6.3112 | 0.0039831 | 5.2908 |
| | SCSSA-VMD-ARIMA-BP | 1.0529 | 0.0001108 | 0.8904 |
| MCORS06 | ARIMA | 1.7966 | 0.003228 | 1.5076 |
| | BP | 3.1568 | 0.009965 | 1.6678 |
| | SCSSA-VMD-ARIMA | 1.1310 | 0.001279 | 1.0385 |
| | SCSSA-VMD-BP | 1.8952 | 0.003592 | 1.4600 |
| | SSA-VMD-ARIMA-BP | 1.2840 | 0.001649 | 1.0819 |
| | SCSSA-VMD-ARIMA-BP | 0.7847 | 0.0006157 | 0.7029 |
| MCORS07 | ARIMA | 2.3492 | 0.005519 | 2.0234 |
| | BP | 1.0872 | 0.001182 | 0.6648 |
| | SCSSA-VMD-ARIMA | 1.3797 | 0.001903 | 1.1796 |
| | SCSSA-VMD-BP | 0.9178 | 0.000842 | 0.8801 |
| | SSA-VMD-ARIMA-BP | 2.2488 | 0.005057 | 1.8573 |
| | SCSSA-VMD-ARIMA-BP | 0.7197 | 0.0005179 | 0.6539 |
| MCORS08 | ARIMA | 0.9810 | 0.0009643 | 0.7512 |
| | BP | 2.2736 | 0.0051693 | 2.0039 |
| | SCSSA-VMD-ARIMA | 0.6135 | 0.0003764 | 0.5474 |
| | SCSSA-VMD-BP | 1.0698 | 0.0011445 | 0.9839 |
| | SSA-VMD-ARIMA-BP | 0.5242 | 0.0002748 | 0.4165 |
| | SCSSA-VMD-ARIMA-BP | 0.4635 | 0.0002148 | 0.4186 |

7. Conclusions

Addressing the challenges posed by the nonlinearity and non-stationary interference in GNSS monitoring data, along with the various types of noise generated during data acquisition, the accurate prediction of surface subsidence becomes a complex task. This paper introduces a hybrid prediction method, namely, the SCSSA-VMD-SE-ARIMA-BP model. In summary, the SCSSA-VMD technique is utilized to decompose the original GNSS monitoring data sequence, thereby enhancing the predictability of the sequence. Subsequently, based on the sample entropy values of each sub-sequence, judgments are made, and the sub-sequences are reconstructed accordingly. Finally, different prediction models, ARIMA and BP, are applied to forecast the reconstructed sequences separately, and their respective predictions are aggregated to obtain the final prediction. Furthermore, the performance of the proposed model is validated by comparing it with various benchmark models. The key conclusions are as follows:

- (1) Upon proposing a novel optimization approach named the Sine Cosine Algorithm with a refraction reverse-learning mechanism and incorporating a Cauchy mutation strategy into SSA, we introduce the resulting method, referred to as SCSSA, to optimize VMD. Comparative analysis with other optimization algorithms reveals that SCSSA exhibits superior performance, characterized by faster convergence speed and higher optimization accuracy.
- (2) By utilizing the optimized VMD in an adaptive manner, the subsidence data sequences from the monitoring stations were effectively decomposed. The results indicate that SCSSA-VMD, when compared to other data preprocessing methods, demonstrates robust resistance to noise interference and maintains stable predictive performance.
- (3) Based on the SE values of the decomposed subsequences, effective data reconstruction can be achieved. The reconstructed sequences were forecasted using both the ARIMA

model and the BP neural network model. The experimental results demonstrate that this approach further enhances prediction accuracy.

- (4) The experiments were independently conducted on data from the four GNSS monitoring stations on the 110801 working face. The experimental results indicate that SCSSA-VMD-SE-ARIMA-BP demonstrates the highest prediction accuracy. Furthermore, it displays excellent applicability across various monitoring station data, facilitating precise predictions for crucial subsidence points in the mining area.

Author Contributions: L.S. designed the algorithm, performed the data processing and analysis, and completed the experimental validation process; W.L. contributed to the formation of the logic and structure of the scientific presentation, the interpretation of the results, and the review of the manuscript. All authors have read and agreed to the published version of the manuscript.

Funding: This research was funded by the Anhui Science and Technology Major Project (Grant No. 202103a05020026); Anhui Provincial Natural Science Foundation Project (No. 2008085MD114); Key Research and Development Plan of Anhui Province (No.: 202104a07020014); Anhui Natural Science Foundation Youth Project (No. 2208085QD115); Anhui Provincial Department of Education Natural Science Key Projects (Number: KJ2020A0311); and National Natural Science Foundation of China (No. 41474026).

Data Availability Statement: Data are contained within the article.

Conflicts of Interest: The authors declare no conflict of interest.

References

- Gao, C.; Xu, N.; Liu, G.; Tian, G. Challenges and opportunities for the development of China's coal industry. *Coal Min. Technol.* **2019**, *24*, 14–29.
- Wang, R. *Research on Multi-Source Data Fusion Technology and Application of Mining Subsidence Monitoring*; China University of Mining and Technology: Xuzhou, China, 2022.
- Tan, X.-Y.; Chen, W.; Wang, L.; Qin, C. Spatial deduction of mining-induced stress redistribution using an optimized non-negative matrix factorization model. *J. Rock Mech. Geotech. Eng.* **2023**, *15*, 2868–2876. [[CrossRef](#)]
- Holdahl, S.R.; Morrison, N.L. Regional investigations of vertical crustal movements in the U.S., using precise relevelings and mareograph data. *Tectonophysics* **1974**, *23*, 373–390. [[CrossRef](#)]
- Monserrat, O.; Crosetto, M. Deformation measurement using terrestrial laser scanning data and least squares 3D surface matching. *ISPRS J. Photogram. Remote Sens.* **2008**, *63*, 142–154. [[CrossRef](#)]
- Wang, H.; Cao, Y.; Wang, G.; Li, P.; Zhang, J.; Gong, Y. Improving Differential Interferometry Synthetic Aperture Radar Phase Unwrapping Accuracy with Global Navigation Satellite System Monitoring Data. *Sustainability* **2023**, *15*, 13277. [[CrossRef](#)]
- Yu, X.; Lv, W.; Ke, F.; Wang, L.; Zhao, X.; Liu, C.; Wang, S.; Zhang, C. *Automatic Monitoring System for Coal Mine Subsidence*; Surveying and Mapping Press: Beijing, China, 2014.
- Lv, W. *Research on the Automatic Monitoring System for Coal Mining Subsidence*; China University of Mining and Technology: Xuzhou, China, 2016.
- Zhang, J.; Qin, Y.; Zhang, X.; Che, G.; Sun, X.; Duo, H. Application of non-equidistant GM(1,1) model based on the fractional-order accumulation in building settlement monitoring. *J. Intell. Fuzzy Syst.* **2022**, *42*, 1559–1573. [[CrossRef](#)]
- Zhou, T.; Jie, Y.; Wei, Y.; Zhang, Y.; Chen, H. A real-time prediction interval correction method with an unscented Kalman filter for settlement monitoring of a power station dam. *Sci. Rep.* **2023**, *13*, 4055. [[CrossRef](#)]
- Hu, B.; Tan, H. Slope deformation analysis and forecast based on ARIMA model. *Bull. Surv. Mapp.* **2019**, *6*, 112–116.
- Kim, Y.; Son, M.; Moon, H.-K.; Lee, S.-A. A study on the development of an artificial neural network model for the prediction of ground subsidence over abandoned mines in Korea. *Geosystem Eng.* **2016**, *20*, 163–171. [[CrossRef](#)]
- Bates, J.M.; Granger, C. The combination of forecasts. *J. Oper. Res. Soc.* **1969**, *20*, 451–468. [[CrossRef](#)]
- Du, S.; Feng, G.; Wang, J.; Feng, S.; Malekian, R.; Li, Z. A New Machine-Learning Prediction Model for Slope Deformation of an Open-Pit Mine: An Evaluation of Field Data. *Energies* **2019**, *12*, 1288. [[CrossRef](#)]
- Han, Y.; Wang, Y.; Liu, C.; Hu, X.; Du, L. Application of regularized ELM optimized by sine algorithm in prediction of ground settlement around foundation pit. *Environ. Earth Sci.* **2022**, *81*, 413. [[CrossRef](#)]
- Xu, G.; Jing, Z.; Mao, Y.; Su, X. A Dam Deformation Prediction Model Based on ARIMALSTM. In Proceedings of the 2020 IEEE Sixth International Conference on Big Data Computing Service and Applications, Oxford, UK, 3–6 August 2020; pp. 205–211. [[CrossRef](#)]
- Kim, D.; Kwon, K.; Pham, K.; Oh, J.-Y.; Choi, H. Surface settlement prediction for urban tunneling using machine learning algorithms with Bayesian optimization. *Autom. Constr.* **2022**, *140*, 104331. [[CrossRef](#)]

18. Kim, D.; Pham, K.; Oh, J.-Y.; Lee, S.-J.; Choi, H. Classification of surface settlement levels induced by TBM driving in urban areas using random forest with data-driven feature selection. *Autom. Constr.* **2022**, *135*, 104109. [[CrossRef](#)]
19. Shahri, A.A.; Pashamohammadi, F.; Asheghi, R.; Shahri, H.A. Automated intelligent hybrid computing schemes to predict blasting induced ground vibration. *Eng. Comput.* **2021**, *38*, 3335–3349. [[CrossRef](#)]
20. Nguyen, H.; Choi, Y.; Bui, X.-N.; Nguyen-Thoi, T. Predicting Blast-Induced Ground Vibration in Open-Pit Mines Using Vibration Sensors and Support Vector Regression-Based Optimization Algorithms. *Sensors* **2019**, *20*, 132. [[CrossRef](#)] [[PubMed](#)]
21. Moghaddasi, M.R.; Noorian-Bidgoli, M. ICA-ANN, ANN and multiple regression models for prediction of surface settlement caused by tunneling. *Tunn. Undergr. Space Technol.* **2018**, *79*, 197–209. [[CrossRef](#)]
22. Tang, L.; Na, S. Comparison of machine learning methods for ground settlement prediction with different tunneling datasets. *J. Rock Mech. Geotech. Eng.* **2021**, *13*, 1274–1289. [[CrossRef](#)]
23. Su, J.; Wang, Y.; Niu, X.; Sha, S.; Yu, J. Prediction of ground surface settlement by shield tunneling using XGBoost and Bayesian Optimization. *Eng. Appl. Artif. Intell.* **2022**, *114*, 105020. [[CrossRef](#)]
24. Liu, X.; Hussein, S.H.; Ghazali, K.H.; Tung, T.M.; Yaseen, Z.M. Optimized Adaptive Neuro-Fuzzy Inference System Using Metaheuristic Algorithms: Application of Shield Tunneling Ground Surface Settlement Prediction. *Complexity* **2021**, *2021*, 6666699. [[CrossRef](#)]
25. Tan, X.; Chen, W.; Wang, L.; Tan, X.; Yang, J. Integrated Approach for Structural Stability Evaluation Using Real-Time Monitoring and Statistical Analysis: Underwater Shield Tunnel Case Study. *J. Perform. Constr. Facil.* **2020**, *34*, 04019118. [[CrossRef](#)]
26. Nourani, V.; Partoviyani, A. Hybrid denoising-jittering data pre-processing approach to enhance multi-step-ahead rainfall-runoff modeling. *Stoch. Environ. Res. Risk Assess.* **2018**, *32*, 545–562. [[CrossRef](#)]
27. Zhang, J.; Cheng, Z. Prediction of Surface Subsidence of Deep Foundation Pit Based on Wavelet Analysis. *Processes* **2022**, *11*, 107. [[CrossRef](#)]
28. Luo, X.; Gan, W.; Wang, L.; Chen, Y.; Meng, X. A Prediction Model of Structural Settlement Based on EMD-SVR-WNN. *Adv. Civ. Eng.* **2020**, *2020*, 8831965. [[CrossRef](#)]
29. Lin, Z.; Ji, Y.; Liang, W.; Sun, X. Landslide Displacement Prediction Based on Time-Frequency Analysis and LMD-BiLSTM Model. *Mathematics* **2022**, *10*, 2203. [[CrossRef](#)]
30. Guo, Z.; Chen, L.; Gui, L.; Du, J.; Yin, K.; Do, H.M. Landslide displacement prediction based on variational mode decomposition and WA-GWO-BP model. *Landslides* **2019**, *17*, 567–583. [[CrossRef](#)]
31. Lu, T.; Xie, J. Deformation Monitoring Data De-Noising Method Based on Variational Mode Decomposition Combined with Sample Entropy. *J. Geod. Geodyn.* **2021**, *41*, 1–6.
32. Wang, C.; Guo, W. Prediction of Landslide Displacement Based on the Variational Mode Decomposition and GWO-SVR Model. *Sustainability* **2023**, *15*, 5470. [[CrossRef](#)]
33. Chen, X.; Yang, Z.; Tian, Z.; Yang, B.; Liang, P. Denoising Method for GNSS Time Series Based on GA-VMD and Multi-scale Permutation Entropy. *Geomat. Inf. Sci. Wuhan Univ.* **2023**, *48*, 1425–1434.
34. Yao, G.; Wang, Y.; Benbouzid, M.; Ait-Ahmed, M. A Hybrid Gearbox Fault Diagnosis Method Based on GWO-VMD and DE-KELM. *Appl. Sci.* **2021**, *11*, 4996. [[CrossRef](#)]
35. Gao, X.; Guo, W.; Mei, C.; Sha, J.; Guo, Y.; Sun, H. Short-term wind power forecasting based on SSA-VMD-LSTM. *Energy Rep.* **2023**, *9*, 335–344. [[CrossRef](#)]
36. Liu, H.; Zhang, X. AQI time series prediction based on a hybrid data decomposition and echo state networks. *Environ. Sci. Pollut. Res.* **2021**, *28*, 51160–51182. [[CrossRef](#)] [[PubMed](#)]
37. Dragomiretskiy, K.; Zosso, D. Variational Mode Decomposition. *IEEE Trans. Signal Process.* **2014**, *62*, 531–544. [[CrossRef](#)]
38. Xue, J.; Shen, B. A novel swarm intelligence optimization approach: Sparrow search algorithm. *Syst. Sci. Control. Eng.* **2020**, *8*, 22–34. [[CrossRef](#)]
39. Tizhoosh, H. Opposition-Based Learning: A New Scheme for Machine Intelligence. In Proceedings of the International Conference on Computational Intelligence for Modelling, Control and Automation and International Conference on Intelligent Agents, Web Technologies and Internet Commerce (CIMCA-IAWTIC'06), Vienna, Austria, 28–30 November 2005. [[CrossRef](#)]
40. Mirjalili, S. SCA: A Sine Cosine Algorithm for solving optimization problems. *Knowl.-Based Syst.* **2016**, *96*, 120–133. [[CrossRef](#)]
41. Li, A.; Quan, L.; Cui, G.; Xie, S. Sparrow search algorithm combining sine-cosine and Cauchy variation. *Comput. Eng. Appl.* **2022**, *58*, 91–99.
42. Ling, Q.; Zhang, Q.; Zhang, J.; Kong, L.; Zhang, W.; Zhu, L. Prediction of landslide displacement using multi-kernel extreme learning machine and maximum information coefficient based on variational mode decomposition: A case study in Shaanxi, China. *Nat. Hazards* **2021**, *108*, 925–946. [[CrossRef](#)]
43. Li, X.; Huang, Z.; Liu, S.; Wu, J.; Zhang, Y. Short-Term Subway Passenger Flow Prediction Based on Time Series Adaptive Decomposition and Multi-Model Combination (IVMD-SE-MSSA). *Sustainability* **2023**, *15*, 7949. [[CrossRef](#)]
44. Bevis, M.; Businger, S.; Herring, T.A.; Rocken, C.; Anthes, R.A.; Ware, R.H. GPS meteorology: Remote sensing of atmospheric water vapor using the global positioning system. *J. Geophys. Res. Atmos.* **1992**, *97*, 15787–15801. [[CrossRef](#)]
45. Jian, L. *Research on the Method of Settlement Analysis of Geodetic Height in GPS Deformation Monitoring*; Kunming University of Science and Technology: Kunming, China, 2015.
46. Huang, X.; Cao, H.; Jia, B. Optimization of Levenberg Marquardt Algorithm Applied to Nonlinear Systems. *Processes* **2023**, *11*, 1794. [[CrossRef](#)]

47. Asheghi, R.; Hosseini, S.A.; Saneie, M.; Shahri, A.A. Updating the neural network sediment load models using different sensitivity analysis methods: A regional application. *J. Hydroinformatics* **2020**, *22*, 562–577. [[CrossRef](#)]
48. Dupuis, E.; Novo, D.; O'Connor, I.; Bosio, A. Sensitivity Analysis and Compression Opportunities in DNNs Using Weight Sharing. In Proceedings of the 2020 23rd International Symposium on Design and Diagnostics of Electronic Circuits & Systems (DDECS), Novi Sad, Serbia, 22–24 April 2020; pp. 1–6. [[CrossRef](#)]
49. Battaglia, E.; Bioglio, L.; Pensa, R.G. Towards Content Sensitivity Analysis. In *Advances in Intelligent Data Analysis XVIII*; Berthold, M., Feelders, A., Kreml, G., Eds.; IDA 2020; Lecture Notes in Computer Science; Springer: Cham, Switzerland, 2020; Volume 12080.
50. Shahri, A.A.; Chunling, S.; Larsson, S. A hybrid ensemble-based automated deep learning approach to generate 3D geo-models and uncertainty analysis. In *Engineering with Computers*; Springer: London, UK, 2023; pp. 1–16. [[CrossRef](#)]

Disclaimer/Publisher's Note: The statements, opinions and data contained in all publications are solely those of the individual author(s) and contributor(s) and not of MDPI and/or the editor(s). MDPI and/or the editor(s) disclaim responsibility for any injury to people or property resulting from any ideas, methods, instructions or products referred to in the content.